Medical Engineering and Physics 58 (2018) 1–12

Contents lists available at ScienceDirect

Medical Engineering and Physics

journal homepage: www.elsevier.com/locate/medengphy

How can a short stem hip implant preserve the natural, pre-surgery force flow? A finite element analysis on a collar cortex compression concept (CO^4)

B. Eidel[a,*], A. Gote[a], A. Ohrndorf[b], H.-J. Christ[b]

[a] Heisenberg-Group, Universität Siegen 57068 Siegen, Paul-Bonatz-Str. 9–11, Germany
[b] Institut für Werkstofftechnik, Universität Siegen, 57068 Siegen, Paul-Bonatz-Str. 9–11, Germany

ARTICLE INFO

Article history:
Received 15 May 2017
Revised 17 March 2018
Accepted 16 April 2018

Keywords:
Biomechanics
Hip endoprosthesis
Force transmission
Interfaces
Stress shielding
Finite element analysis

ABSTRACT

The present work proposes a simple, novel fixation concept for short stem hip endoprostheses, which preserves the pre-surgery force flow through femoral bone to an unprecedented extent. It is demonstrated by finite element analyses that a standard implant model endowed with minor geometrical changes can overcome bone loading reduction and can achieve almost physiological conditions. The numerical results underpin that the key aspect of the novel, so-called “collar cortex compression concept CO^4” is the direct, almost full load transmission from the implant collar to the resected femur cortex, which implies that the implant stem must be smooth and therefore interacts mainly by normal contact with the surrounding bone. For a stem endowed with surface porosity at already small areas, it is mainly the stem which transmits axial forces by shear, whereas the collar shows considerable unloading, which is the standard metaphyseal fixation. Only in the latter case the implant-bone stiffness contrast induces stress shielding, whereas for CO^4 stress shielding is avoided almost completely, although the implant is made of a stiff Ti-alloy. CO^4 is bionics-inspired in that it mimics force transmission at implant-bone interfaces following the natural conditions and it thereby preserves pre-surgery bone architecture as an optimized solution of nature.

1. Introduction

The structure of bone follows from adaptation to predominant loading conditions. Total hip arthroplasty (THA) replaces femur parts by an implant and changes the load transfer by the implant-bone interface and thereby largely determines the consecutive force flow through the femur. As a consequence, the post-surgery force flow through bone induces stimuli for remodeling; bone resorption along with stiffness loss takes place in regions of lower loading, an increase of bone density and stiffness is induced in regions of higher loading. For bone resorption in the vicinity to the implant, aseptic implant loosening is imminent, which then calls for revision surgery.

Stress mediated bone resorption is caused by stress shielding. It is primarily attributed to the stiffness mismatch between implant and bone, which is the literal meaning of stress shielding, [1]; when two materials are joined and undergo homogeneous straining in the direction of the material interface, the stiffer material bears the majority of the load. In a broader sense stress shielding refers to stress reduction in bone, no matter by which means. Then, it also covers the effect of particular load application from implant to bone, which shows considerable differences between different implant concepts.

For the cementless, short-stem femoral fixation concepts in THA [2,3], Fig. 1 sketches three different variants of force transfer, where we restrict to forces in the direction of the axis of the implant's stem, normal forces are not displayed. The first version, Fig. 1 (a), represents the very standard; a metaphyseal anchored short stem implant which exhibits an implant-to-bone force transfer via shear due to the stem's porous surface allowing for osseointegration.

Fig. 1(b) displays the qualitative load transfer/fixation concept, when the implant version (a) is enhanced by a collar plate. In that case the implant-to-bone force transfer is partitioned between the stem and the collar.

While for standard case (a) the axial force is completely transmitted through the implant's stem via shear, the case of Fig. 1 (c)

* Corresponding author.
E-mail addresses: bernhard.eidel@uni-siegen.de, bernhard.eidel@googlemail.com (B. Eidel).

https://doi.org/10.1016/j.medengphy.2018.04.016
1350-4533/

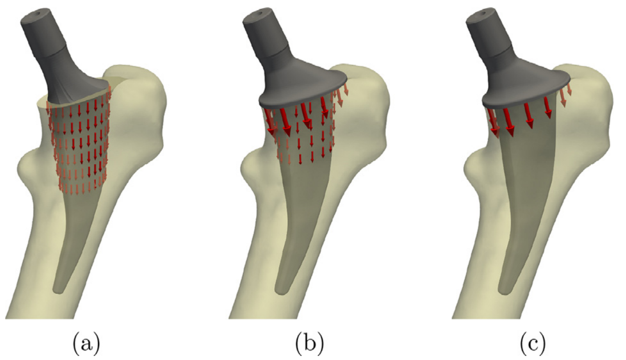

Fig. 1. Variants of implant-to-bone force transfer for cementless short stem hip endoprostheses: (a) Shear stress dominated force transfer through the stem's porous surface, (b) a mixed force transfer concept combining force transmission via collar and via stem (c) the collar cortex compression concept CO^4, where it is the collar that completely transmits the axial force and the smooth stem interacts with bone purely by normal stress.

shall play the counterpart to case (a) in that the force acting in axial direction is purely transmitted by the collar through normal, compressive stress; this particular load transfer is restricted to the collar on purpose and realized by a stem surface, which is ideally smooth such that no shear stresses can be transmitted through the bone-implant contact area. The stem interacts with the surrounding bone by normal contact and thereby stabilizes the implant's position. We call this particular, unconventional concept the "collar cortex compression concept" CO^4. It is to the best of our knowledge not realized in any variant of the existing short stem implants.

If the load application resembles the natural, pre-surgery conditions, the stimuli for remodeling towards structural changes in bone composition are minimized. This can be seen as a bionics inspired design rule. It does not refer to reducing the implant-bone stiffness contrast, either by more compliant materials [4–6] or by reducing the moment of inertia [7] e.g. by mimicking the natural material of spongy bone by a cellular structure as previously done [8]. Instead, the bionics perspective is to preserve the natural force flow by force transmission from implant-to-bone by appropriate boundary or interface conditions. Then the existing bone architecture as a result of bone's adaptation to the prevailing loading conditions is preserved. Hence, the present work does not aim to contribute to the field of remodeling, but to the analysis of conditions that preserve pre-THA bone composition.

Hip implant design striving for a direct, full load transfer at the resected femur was already introduced by Huggler and Jacob [9] in terms of a thrust plate prosthesis (TPP). With a focus on remodeling this concept was subsequently analyzed in finite element simulations [10] and mid-term experiences with TPPs are already available [11].

With the aim of a physiological load transmission an implant type was proposed [12,13] that combines a proximal compression plate with cables that anchor the prosthesis to the bone and thereby mechanically activate the greater trochanter. This concept, however, has not entered the surgery practice of THA.

The objective of the present work is to analyze our newly introduced implant concept CO^4 and to compare it with the standard concept of Fig. 1 (a). More in detail we investigate by a finite element analysis distinct concepts of load transmission from implant-to-bone. We choose a well-established model of a collarless short stem endoprosthesis following the shear load transmission concept. By the enhancement of a collar to that implant we study the transition in force transmission towards the scenario with full force flow through the collar. The driver for this gradual transition is the amount of surface area at the implant stem containing pores into which osteoblasts and supporting connective tissue can migrate.

The overall aim is to identify the implant variant that comes closest to the presurgery force flow. Interestingly, the analysis enables a fresh new look on the issue of stress shielding.

2. Materials and methods

2.1. Femur reconstruction

The CAD-model of the femur was generated using Avizo 3D, version 9.0.1 (FEI Company, Hillsboro, Oregon, USA). The computer tomography (CT) data used for the present study were obtained from the Visible Human Project [14,15], and belong to a 59 year old female cadaver. Three data sets for hip, knee and pelvis with altogether 432 CT images in DICOM (Digital Imaging and Communications in Medicine) format were merged for the femur reconstruction. Every image has a resolution of 512×512 pixels and 12 bit gray scales. The images are vertically spaced with a distance of 0.33 mm. The vertical distance equals the horizontal distance between the pixels, which allows for the use of cubic voxels for reconstructing the femur.

Fig. 2 displays the workflow from CT scans to the finite element bone model. In (a), the segmentation process of the bone from the CT images is exemplarily shown for one slice; in the first stage (i) the initial CT image is reduced in size and contrast is increased, in the next stage (ii) segmentation is carried out after applying a thresholding algorithm. In stage (iii) the segmentation follows manually editing, and (iv) the selection of surface data for export completes the process. Furthermore, Fig. 2 displays the consecutive steps, (b) the staple of CT-images, (c) a preliminary surface mesh of the femur that still exhibits some surface edges as artifacts originating from surface reconstruction by means of 2D data, (d) the smoothed surface model, and finally, (e) the finite element discretization along with boundary conditions. Recently, a fully automated segmentation method was introduced, which is accurate, robust and automatic [16].

The strongly heterogeneous Young's modulus distribution is obtained from the CT images in three steps. First, the *CT* number, which exhibits the so-called Hounsfield unit (HU), is calculated for bony tissue by means of the attenuation coefficients μ of bony tissue and water; it holds [17]

$$CT(\mu_{\text{tissue}}) := \frac{\mu_{\text{tissue}} - \mu_{\text{water}}}{\mu_{\text{water}}} \cdot 1000\,\text{HU}. \tag{1}$$

Second, the tissue density ρ_{tissue} is calculated as a function of the *CT* number

$$\rho_{\text{tissue}}(CT) = \frac{\rho_{\text{water}} - \rho_{\text{air}}}{CT_{\text{water}} - CT_{\text{air}}} \cdot CT_{\text{tissue}} + \rho_{\text{water}}. \tag{2}$$

The linear conversion in (2) is based on the observation that the *CT* number scales approximately linearly with the density of the material, and on the knowledge of the *CT* values for water and air.

Third, the Young's modulus is calculated according to the empirical formula [18]

$$E = 6500\,\frac{\text{N}}{\text{mm}^2} \cdot \left(\frac{\rho_{\text{tissue}}}{\rho_0}\right)^2, \tag{3}$$

where ρ_0 is a reference density with $\rho_0 = 1\,\text{g/cm}^3$. There are alternatives to (3), the interested reader is referred elsewhere [19–21]. The above conversions are carried out using a Python script [22].

The data sets for the reconstructed bone model and finite element discretizations are made available as a supplement of the present paper. They shall facilitate research in the field of hip implants in the spirit of previous work [23], where in the frame of a "Standardized Femur Program" the geometry data of a composite femur were published.

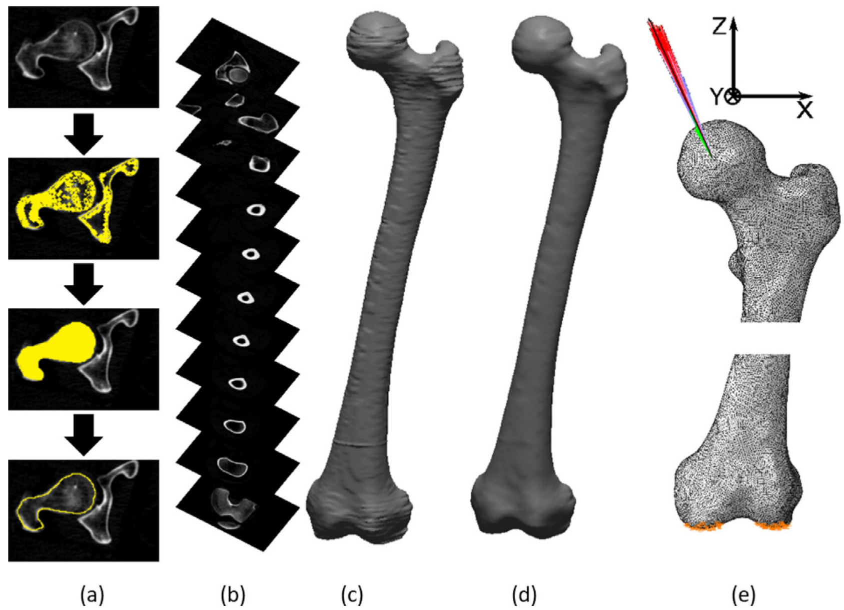

Fig. 2. Workflow for femur reconstruction, from computer tomography (CT) scans to the finite element model: (a) Segmentation of the bone from the CT images, (b) staple of CT-images, (c) preliminary surface mesh, (d) smoothed surface model, (e) finite element discretization with boundary conditions.

Table 1
FEA data for discretizations and material properties: number of finite element nodes and elements, parameters for linear elasticity of implants and bone.

	Endoprosthesis		Bone	
	standardSS	collarSS	Pre-surgical	Post-surgical
No. of nodes	79,493	70,935	991,564	923,529
No. of elements	53,694	47,042	699,816	650,185
Young's modulus E [MPa]	110,000		$\in$ [107.5, 23510.5]	
Poisson's ratio ν	0.33		0.35	

2.2. Finite element analysis

The finite element solver Abaqus 6.14 (Dassault Systèmes, Paris, France) was used in geometrical nonlinear simulations for deformation and stress analyses. Tetrahedral finite elements with quadratic shape functions (10 nodes) along with displacement degrees of freedom were used for the discretization of the femur and the implant. Convergence studies have shown that the chosen discretizations as listed in Table 1 yield virtually converged results.

2.2.1. Material model

For the material behavior of femoral bone, an isotropic linear elasticity law is assumed to hold. The assumption of linear elasticity is corroborated by recent experimental findings [28,29], the validity of isotropic elasticity in simulations is underpinned in previous work [30]. The figures of the strongly heterogeneous Young's modulus distribution in Table 1 follow from bone reconstruction as described in Section 2.1. The Poisson's ratio is assumed to be constant, $\nu = 0.35$. For the implant material, linear elastic, isotropic material parameters of a Ti-alloy (TiAl6V4) are chosen [31].

2.2.2. Variants of short stem hip endoprostheses

In the numerical analysis the following implant variants are considered:

1. A variant that exhibits only very minor geometrical changes compared to the Metha model; it is referred to as "standardSS", $E = 110000$ N/mm^2, $\nu = 0.33$.
2. The same as variant 1, but with a Young's modulus of cortical bone, $E = 6000$ N/mm^2 and $\nu = 0.33$; it is referred to as "bony standardSS".
3. A collar-plate enhanced variant along with different porous surface coverage of n%, where the reference surface area 100% is defined by the Metha model, see Fig. 3 (c). These models are referred to as "collarSS {0/17/29/57/100}%" in the following. Material parameters are the same as for case 1.

Case 1 provides the reference solution for the metaphyseal fixation concept which is the standard force transmission by the stem via shear.

Case 2 is a fictitious one, in which cortical bone is chosen for the implant material for two reasons; first, in order to quantify the impact of the implant-bone stiffness contrast on stress shielding, second, in order to neatly separate the influence of materials stiffness from the impacts of different concepts of implant-to-bone force transfer. Note that for case 2 the Young's modulus is even less than 6% of the Young's modulus of the Ti-alloy.

Case 3 realizes the collar cortex compression concept CO^4 in terms of the model collarSS 0% as sketched in Fig. 1 (c). The variants differ by the amount of the stem's porous surface coverage, which is the key parameter to study the decomposition of force transfer between stem and collar.

2.2.3. Boundary conditions

Dirichlet boundary conditions are chosen at the distal end of the femur that is all degrees of freedom are fixed, see Fig. 2 (e). For the Neumann conditions, only the force acting at the femur head is modeled. The magnitude and direction of the force as displayed in Fig. 2 (e) are chosen for the maximal force during jogging at a pace of 8 km/h according to the data from the free public Orthoload database [24]. The force vector shows relatively small

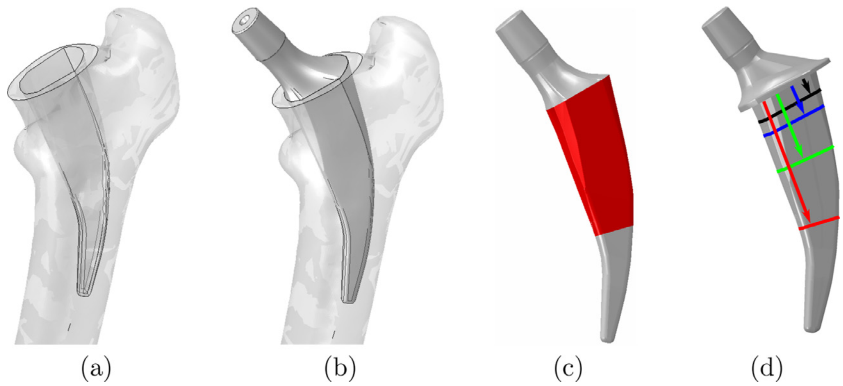

Fig. 3. (a) The resected femur neck with a cavity of the size of the implant stem, (b) the position of the short stem implant, (c) the Metha prosthesis (Aesculap, Tuttlingen, Germany) with its porous stem surface in red color, (d) the collarSS n%, with its different surface areas, $n = \{0, 17, 29, 57, 100\}$ that are covered with a porous layer. (For interpretation of the references to color in this figure legend, the reader is referred to the web version of this article.)

angular variations during one loading step. A detailed description of a hip joint prosthesis that enables in vivo measurements is reported elsewhere [25].

Conditions of perfect bonding/sticking friction are chosen for the porous implant surface with bone. This modeling applies to the collar-plate and to the porous stem surface. The assumption of sticking friction is based on both a press-fit along with a large coefficient of friction (cof) right after THA, and on effective osseointegration on a larger timescale.

For the stem parts without surface porosity, two different cases are considered; frictionless contact, hence cof= 0.0 and cof= 0.25. In the clearly unrealistic frictionless case of Fig. 1 (c) stem and bone merely interact by normal force which is the counterpart to the purely shear-mediated force transfer of the standard stem in Fig. 1 with its –similarly unrealistic– assumption of sticking friction everywhere. A cof= 0.25 for the latter case is very likely to set an upper bound of friction for a Ti-alloy protected by a low-friction Diamond-Like Corbon (DLC) thin film, for details see Section 4.

Notice, that there are considerable uncertainties concerning the frictional contact conditions and the intensity of press-fit [26,27]. In this context, the definition of a common protocol or benchmark setting is still a shared but hardly fulfilled need of the modeling and simulation community.

2.2.4. Measures in the numerical analysis

The strain energy density (SED) is defined by means of the scalar-product of work-conjugate pairs of stress and strain tensors, here the Second Piola–Kirchhoff stress tensor $\boldsymbol{S}$ and the Green–Lagrange strain tensor $\boldsymbol{E}$,

$$\mathrm{SED} = \frac{1}{V}\int_V \boldsymbol{S} : \boldsymbol{E}\, \mathrm{dV}. \tag{4}$$

SED is a widely accepted measure of mechanical stimulus for bone remodeling [4,32], a detailed discussion can be found in the references [33–35].

The relative, percental SED deviation of the post-THA bone from the pre-THA bone is calculated according to

$$\mathrm{SED_{diff}} = \left(\mathrm{SED}^{\mathrm{post-THA}} - \mathrm{SED}^{\mathrm{pre-THA}}\right)/\mathrm{SED}^{\mathrm{pre-THA}}. \tag{5}$$

A similar metric based on von-Mises stress instead of SED was previously used [36,37] and referred to as Stress Shielding Intensity SSI.

For a comparison among the implant variants and with the pre-surgery state the following indicators are used: (i) normal strain and normal stress distributions at the resection plane, (ii) SED differences according to (5), (iii) a partitioning of force transfer into its collar and stem parts. Furthermore, (iv) the analysis is based on SED as well as the shear stress distributions along medial, lateral, ventral and dorsal paths in vicinity to the prosthesis surface.

3. Results

3.1. The load transfer in the natural femur

Predominant loading conditions generally drive the remodeling processes within bone, which have resulted in the Young's modulus distributions as displayed in Fig. 4 (a), (b); this shall be understood as the result of nature's optimization processes. As a consequence, the post-surgical load transfer is *best adapted* to the existing bone-structure and loads, if it induces the *least action of remodeling* towards an altered bone structure. For that reason, preserving the characteristics of pre-THA force transmission through bone is optimal, since it does not drastically alter –lower or increase– local bone loading. This is the particular perspective of the present work and for that reason, pre-THA force transmission is the point of departure.

Fig. 4 illustrates for the pre-surgical femur that the SED distribution follows the Young's modulus distribution. This fact underpins that stiffness attracts strain energy. Since the values of the cortex and the spongiosa differ by orders of magnitude, two different scales are necessary to properly display the distributions of both SED and Young's modulus, see the caption of Fig. 4.

3.2. Load transfer at interfaces

3.2.1. The resection plane

Fig. 5 displays the normal strain and corresponding normal stress distributions at the resection plane for various cases. In the corresponding cross section of pre-surgery bone, the pictures in Fig. 5 (a) indicate that strain is compressive at the medial site and that it exhibits a continuous decrease from the medial to the lateral site. At the lateral site minor tensile strains show up. The corresponding stress distribution exhibits maxima at the medial and the lateral corticalis sites. Hence, the textbook picture of stress distributions in the femur neck being a superposition of a constant compressive stress state with a linear stress distribution from bending is somewhat oversimplified and the main reason for this deviation is the stiffness heterogeneity of bone. The results for the collarSS 0%/CO[4] case are shown in Fig. 5 (b); the normal stress distribution comes relatively close to the natural femur both qualitatively and quantitatively. By its stiffness the collar-plate induces higher compressive strains in the lateral cortex compared with the pre-THA state.

For collarSS 17% as displayed in Fig. 5 (c), the resection plane is already considerably unloaded compared with the case of

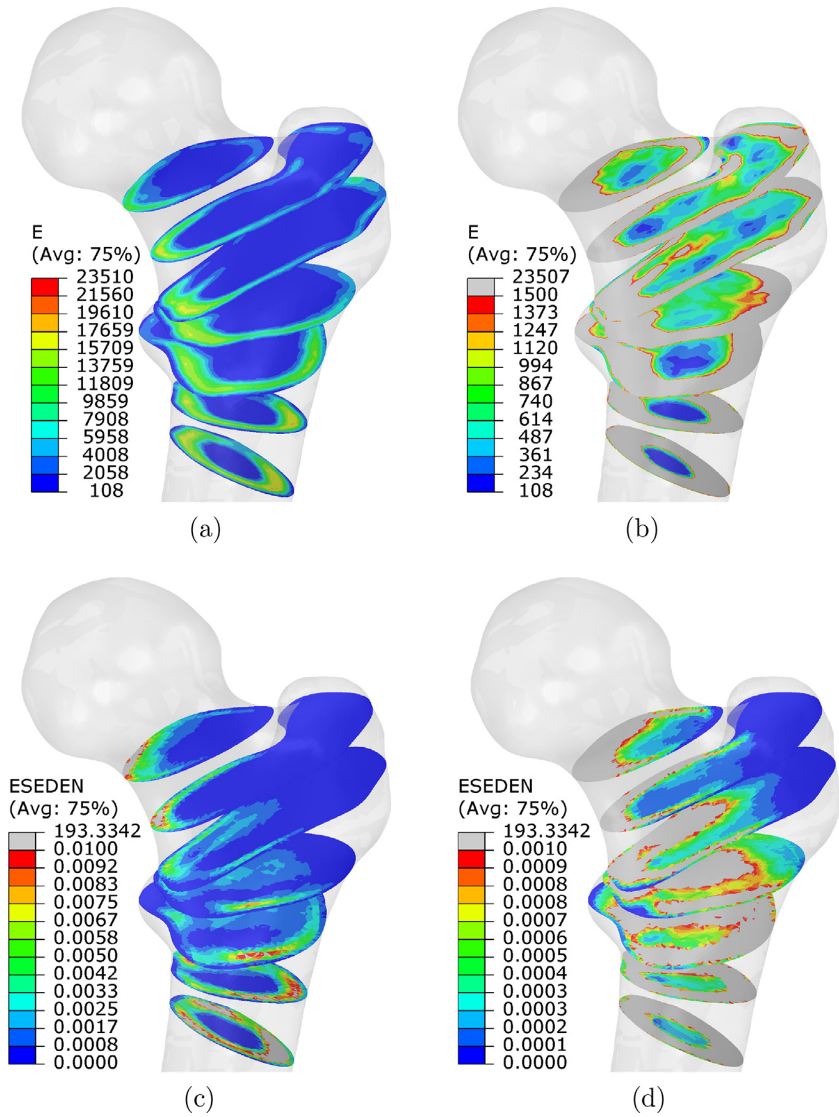

Fig. 4. Distributions of (a, b) Young's modulus [MPa] and (b, c) SED [MPa] in pre-surgery femur: Scaling adapted to cortical bone for (a) Young's modulus and (c) SED. Scaling adapted the spongy bone for (b) Young's modulus and (d) SED.

collarSS 0%; hence, the stem takes over a relatively large portion of the incoming force, although it exhibits surface porosity only at small parts. Of course, for the standard –hence collarless– implant, normal strain and normal stress vanish at the resection face. Instead, the load is purely transferred via shear into spongy bone. Additionally, the implant is blocked by its wedge shape in the tubular corticalis which activates cortical stress in circumferential direction.

Notice that the maximal values of normal stress in Fig. 5 are in the range of the compressive strength of cortical bone, [38,40].

The intermediate conclusion is that the newly introduced CO^4 in terms of the model collarSS 0% shows the best agreement with physiological, pre-THA conditions of force transmission.

3.2.2. *The implant stem*

A closer look into the force transfer at the stem surface for collared implants is shown in Fig. 6 by means of the shear stress component S_{ns} acting along proximal to distal paths in different faces of the stem. The end of the porous surface is indicated by a dashed line; here, shear stress drops to zero value. For the ventral case, Fig. 6 (a), shear stress increases and shows its maximum right at the distal end of surface porosity. For the medial path, Fig. 6 (b), there is a stress peak at the intersection of the collar with the stem for all implant cases. The magnitude of peak stress is inversely proportional to the area of porous surface. A similar behavior is observed for the dorsal implant's face, Fig. 6 (c). For the dorsal path, a peak stress shows rapid decay to the distal end of the porous surface.

Notice that shear stress vanishes identically for collarSS 0%/CO^4 for its perfectly smooth surface as displayed in Fig. 6 (a)–(d).

3.2.3. *Force transfer decomposition*

The previous pictures of load transfer in terms of stress distributions shall be enriched by corresponding forces as integral quantities. Table 2 decomposes the force transmitted by stem and by collar into the directions of the global coordinate system of Fig. 2. For collarSS 0%, hence for a fully smooth stem surface enabling implant-bone interaction purely by normal stress, it is the collar, which transmits 85% of the force in z-direction underpinning, why we coined the term "collar cortex compression concept" CO^4 for this case. Here, the implant stem mainly serves the purpose of safeguarding the position stability through normal contact at the bone-implant interface. For collarSS 17%, i.e. for a relatively small portion of porous surface, the collar-stem F_z force ratio

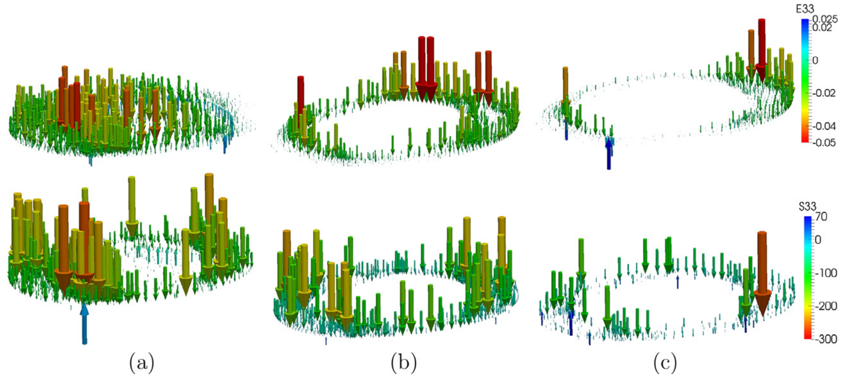

Fig. 5. Force transfer at the resection plane: (Upper row) Normal strain component E_{33} and (bottom row) normal stress component S_{33} (N/mm^2) for (a) the pre-surgery femur, (b) the collarSS 0% i.e. CO[4], and (c) the collarSS 17%. Each in the left is the medial site, each in the front the ventral site.

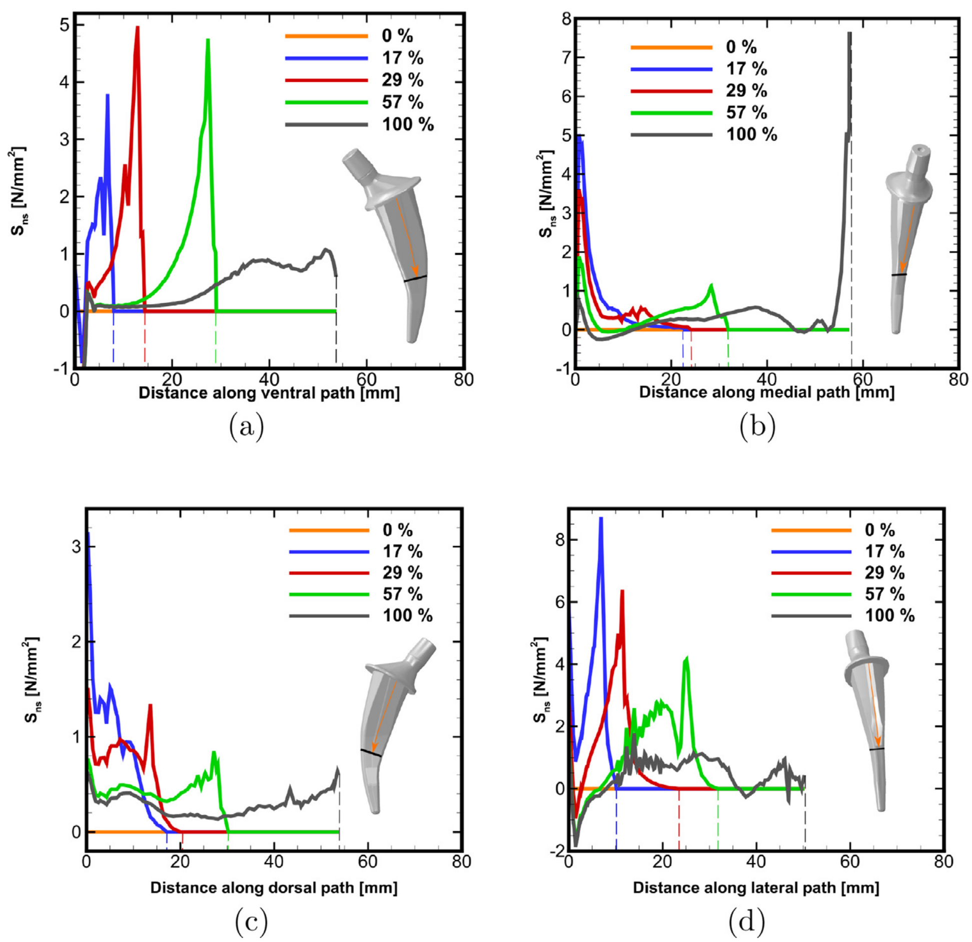

Fig. 6. Shear stress along stem surface paths for collarSS ***n***%: the shear stress component S_{ns} is defined by the path direction s (from proximal to distal) with surface normal n. The dashed line marks the end of the porous surface. For larger s values the shear stress vanishes identically due to the perfectly smooth surface.

Table 2
Load partitioning for collarSS ***n***%: the force ratio collar-to-stem is displayed as a function of the porous surface coverage n and the coefficient of friction cof. The applied force on the femur head is $F_x = 798$, $F_y = 300$, $F_z = -1974$, $|\boldsymbol{F}| = 2150$ in (N).

Force transmission ratio Collar : stem [%]							
Model	Short stem with collar plate						
poros. n [%]	0	17	29	57	100	0	
cof	0.0					0.1	0.25
F_z	85:15	29:71	17:83	11:89	9:91	69:31	64:36
F_x	67:33	23:77	20:80	15:85	10:90	77:23	76:24
F_y	72:28	29:71	21:79	19:81	16:84	79:21	82:18

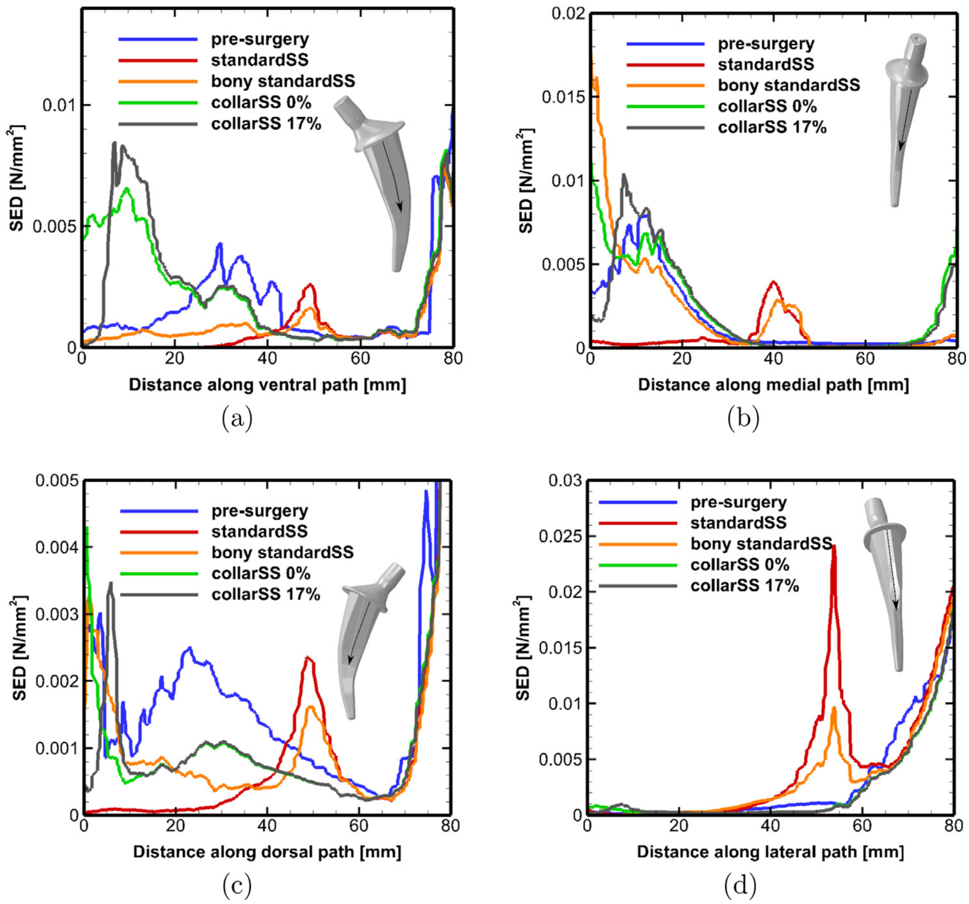

Fig. 7. SED values close to the stem surface: along (a) ventral, (b) medial, (c) dorsal and (d) lateral paths, each from proximal to distal.

shows a significant change to 29:71%. For a further increase of the porous surface coverage up to 100%, the force ratio in z-direction shows moderate changes and ends up at 9:91%. Similarly, the ratios for force components F_x and F_y each exhibit an abrupt change from collarSS 0% to collarSS 17%. These force ratios end up for collarSS 100% at values close to the ratio for the z-component.

The assumption of zero friction at the stem's smooth surface sets the lower bound for the influence of friction. For oxidized surfaces of Ti-alloys in contact with bone coefficients of friction values have been measured ranging from 0.2 to 0.7 [39]. The oxidization in this reference however was carried out on purpose in order to increase friction. In the concept study of the present work an intentionally smooth surface is employed, for which e.g. biocompatible Diamond-Like Carbon (DLC) films can be used for their considerably smaller cof values in the range of 0.05–0.2, for details see Section 4. The corresponding simulation results of force decomposition are displayed in the last two columns of Table 2. As a result, even for a cof$=0.25$ the major part of the applied force in z-direction is transferred by the collar. Interestingly, the F_x and F_y components transmitted by the collar even increase for CO^4 along with nonzero cof.

3.3. The loading of bone

SED distributions in bone close to the implant-bone interface are displayed in the diagrams of Fig. 7. The SED in these regions are critically influenced by an implant through stress shielding. The following observations can be made.

(i) For the SED distributions of collarSS 0% and for collarSS 17% two prominent features are obvious; first, they qualitatively follow the Young's modulus distributions displayed in Fig. 8, which is true for all paths. Second, they come much closer to the pre-surgical conditions than the standardSS.

(ii) The standard implant without collar –both for Ti- and for bony elasticity parameters– exhibits pronounced SED peaks right at the distal ends ($s \approx 50$ mm) of the porous surface. This characteristics, which is seen for all paths, is in contrast to the pre-THA state.

(iii) The implant's elastic stiffness crucially influences the SED, most notably in medial and dorsal paths for $s \in [0, 40]$ mm; while the Ti-based short stem exhibits SED values close to zero, the standard short stem of bony elasticity exhibits large SED values thus coming closer to the pre-THA distributions. Remarkably, in this characteristics it comes closer to the cases of collarSS 0%/17%. The conclusion is that SED reduction can be avoided at some sites by different means, either by reducing the implant-bone stiffness contrast in the shear-mediated force transmisson, or by the newly introduced CO^4.

Fig. 9 displays the distributions of the SED differences compared with pre-THA state (definition of SED_{diff} in (5)) in various proximal cross sections for (a) the standard short stem, for (b) the standard short stem endowed with bone stiffness, for (c) collarSS 0%/ CO^4, and for (d) the collarSS 100%. The results of this panoramic view, which complement the data of Fig. 7 are most telling; the most salient characteristics can be summarized as follows.

(a) For standardSS (Ti-alloy) as displayed in Fig. 9 (a), the SED is considerably reduced in the cortical ring surrounding the implant stem in the first four proximal cross sections. Only the bone regions at the distal surface of the implant exhibit a minor SED reduction, or partially even an SED increase.

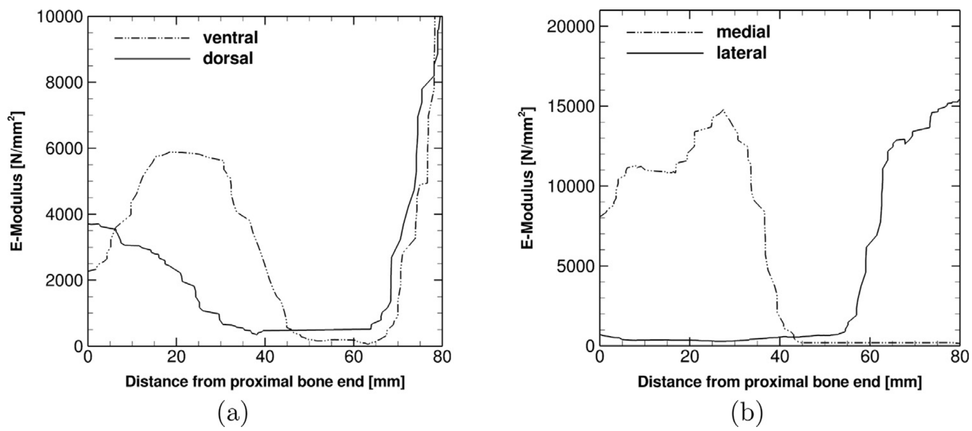

Fig. 8. Young's modulus along the different paths of SED evaluation: (a) ventral and dorsal, (b) medial and lateral, each from proximal to distal.

(b) For standardSS endowed with bone-elasticity, Fig. 9 (b), the SED distribution is much closer to pre-THA conditions than for the Ti alloy, most notably in the proximal dorsal region (Sections 2–4). Here, the effect of stress shielding is at least reduced by a lowered implant-bone stiffness contrast. However, regions of considerable SED reduction persist at ventral surface parts of Sections 2–4, from the medial center into the greater trochanter, and at the resection face. This SED-reduction is caused by the type of implant-bone force transmission via shear.

(c) For collarSS 0%/CO^4, the results in Fig. 9 (c) show almost everywhere no considerable unloading compared with the pre-THA state. Instead, a considerable SED increase is observed in the greater trochanter of the proximal Sections 2 and 3. The SED increase beyond 100% (gray in the color maps of the left column of Fig. 9) is shown in the right column of Fig. 9 using modified scales. The very strong relative SED increase is caused by very low absolute SED values in the pre-THA state. The post-THA SED values however, do not induce plastic deformations for a compressive strength of cortical bone in the range of approximately 250 N/mm^2 [40].

(d) The combination of a collared implant along with a stem fully covered by porosity, i.e. collarSS 100%, exhibits the strongest stress shielding effect in terms of SED reduction; hence a fixation concept following “much is better” yields unfavorable results.

Fig. 10 shows the SED difference for CO^4 along with nonzero friction coefficients. It can be observed that the greater trochanter is less stressed for nonzero cof compared to CO^4 along with cof= 0. Notwithstanding, the reduction in loading compared to the presurgery state is confined to a very small region. In conclusion, CO^4 along with more realistic friction coefficients avoids considerable unloading compared to presurgery conditions and performs much better than the standard implant, since considerable SED reduction is avoided almost everywhere.

4. Discussion

Motivated by the question on how post-surgery force flow can preserve the favorable characteristics of natural pre-surgery conditions, the main aim of the present work was the numerical analysis of force transmission at implant-to-bone interfaces and the study of its impacts on bone loading in comparison to the pre-surgery state.

It has been demonstrated that a collared short stem implant transfers the major part of the applied force to bone by the collar, only if the stem is smooth and thus interacts with bone mainly by normal contact while shear stress in the interface remains small due to low friction coefficients Table 2. In this non-standard case, which is called the collar cortex compression concept CO^4, virtually no femur region shows pronounced SED reduction, Fig. 9 (c), such that bone resorption is not to be expected.

The force partitioning at implant-bone interfaces in Table 2 indicates that (i) the compressive stress dominated force transfer by the collar and the shear stress dominated force transfer by the stem can be reconciled in terms of an arbitrarily tuned force decomposition. However, (ii) the collar is considerably unloaded and forces shifted to the stem-bone interface, if the stem exhibits already a small portion of porous surface that enables osseointegration and therefore force transmission by shear.

As a consequence of the implant cavity, the femur cross section that transmits load is reduced and a higher risk of fracture vulnerability seems to be likely for CO^4, since the load is fully transmitted in the resection plane. Fig. 5 however indicates that the post-surgical loading does not considerably exceed the pre-surgical one. The reason is that the cavity for the implant shaft is mainly in the relatively soft spongiosa, whereas the stiff cortical ring is not reduced by the cavity.

The collar is clearly not an invention of the present work, instead it has been used earlier in various hip endoprothesis models, although it is currently very rare for short stem implants [2]. The functionality of collars is different in traditional concepts compared with CO^4. Previously, the collar mainly served as an additional safety component of the mainly stem-based fixation concept, namely to avoid migration of the implant into the femur. In CO^4 however the collar is not a stand-by or partially activated component, but the only agency of axial force transmission. Vice versa, the stem exhibits a change in functionality on purpose; its loss of surface roughness and porosity implies both no osseointegrationa and a considerable loss of friction. If the stem no longer serves the purpose of force transmission by shear through its surface, but mainly to ensure the position stability via normal stresses at the bone-implant interface, the design of its geometry is free to be optimized according to other design rules as e.g. bone preservation. Notwithstanding, for CO^4 the stem remains a key agency in the metaphyseal fixation opposed to stemless implant versions [41].

The above discussion underpins that CO^4 is not simply a geometrical variant of existing implants, but a novel load transmission concept, where stem and collar undergo a change in functionality.

The process of remodeling is strongly dependent on different mechanical stimuli, biochemical processes showing considerable scatter between human individuals and additionally depending on age, sex and individual disposition. As a consequence, models for

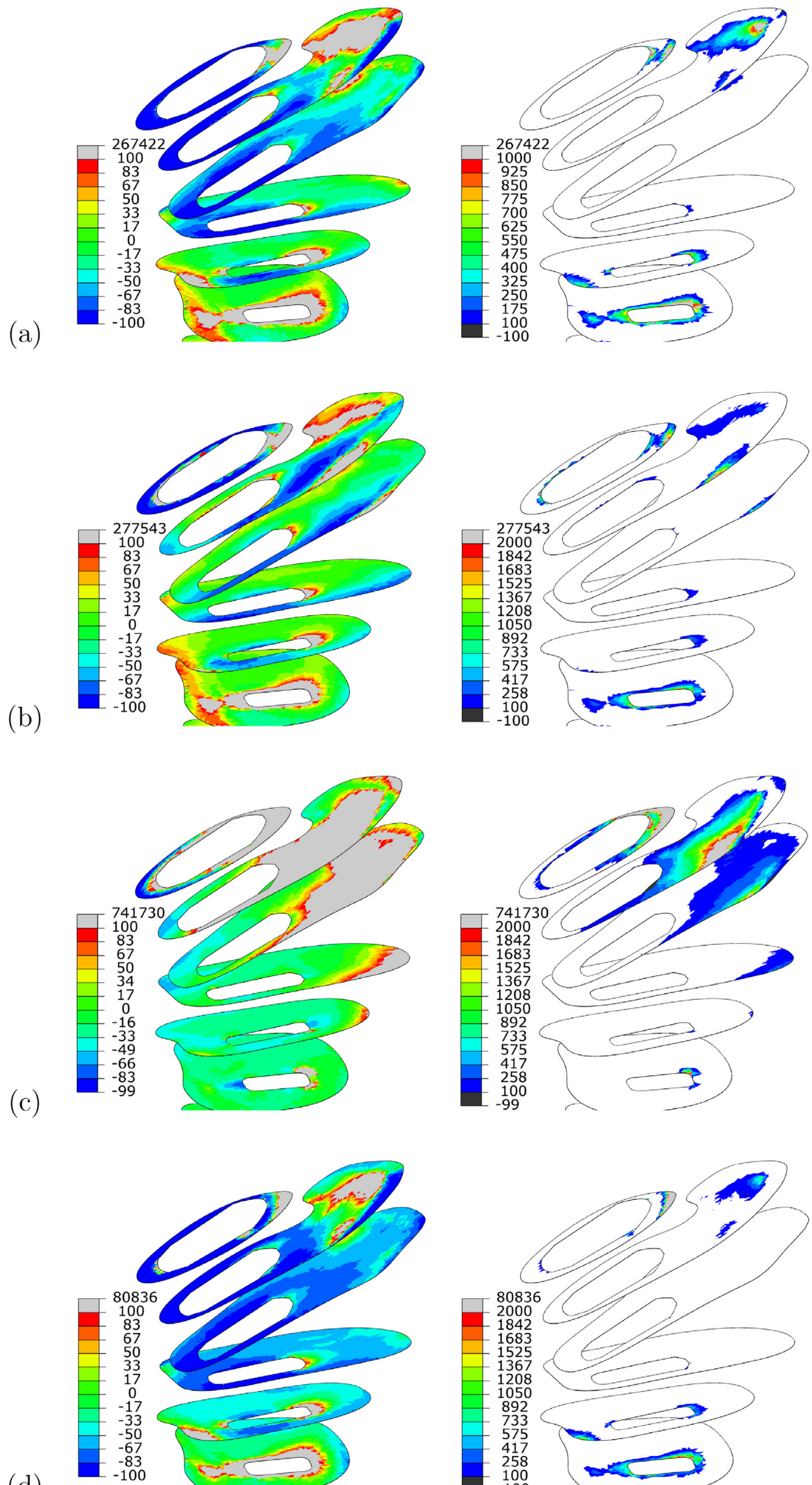

Fig. 9. Relative percentaged SED differences between post-THA and pre-THA state: for (a) standardSS, (b) standardSS endowed with bone stiffness, (c) collarSS 0%/ CO[4], and for (d) collarSS 100%. (Left) Color encoded SED_{diff} in the interval [−100%, 100%], and (right) beyond +100%.

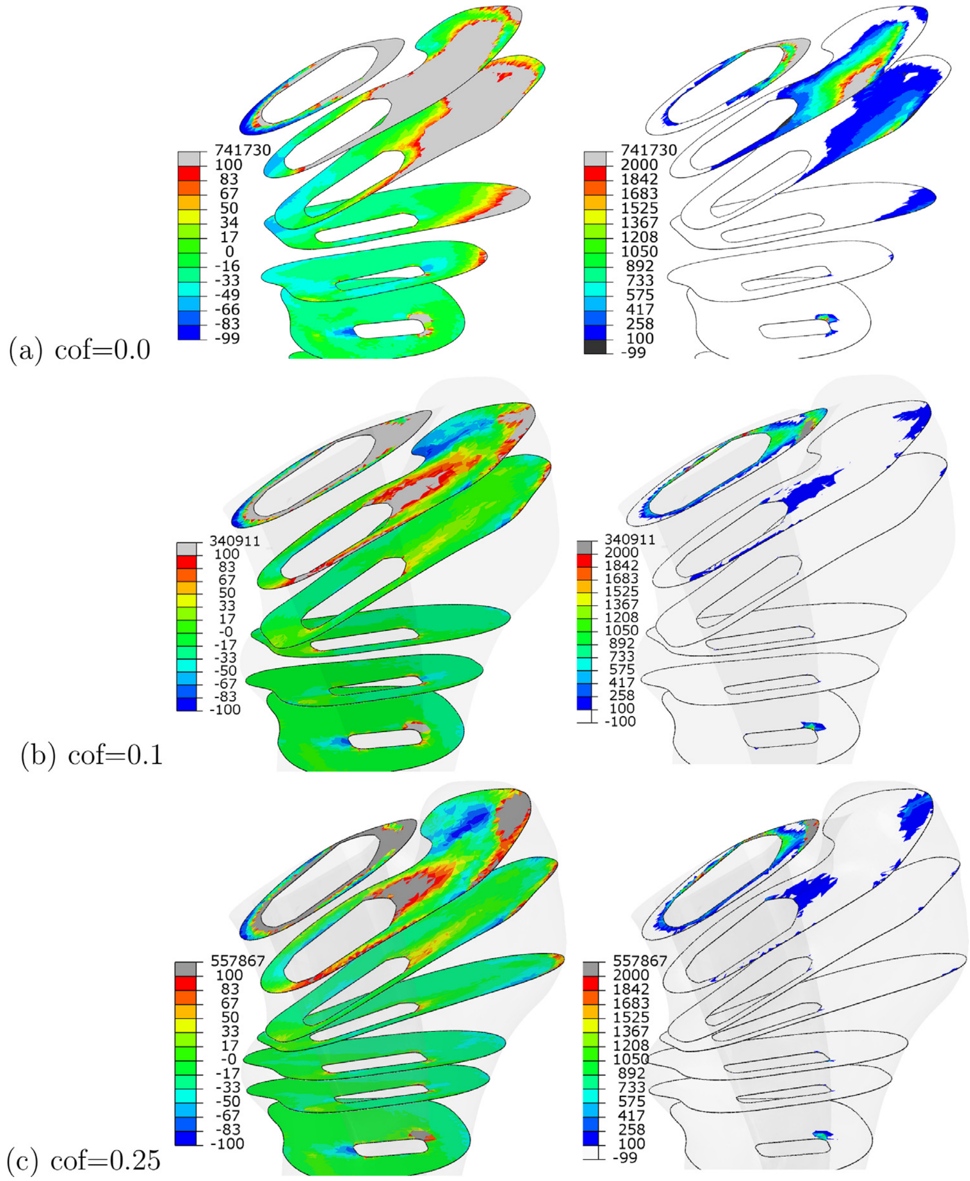

Fig. 10. Relative percentaged SED differences between post-THA and pre-THA state for frictional contact: for (a) cof=0.0, (b) cof=0.1, and for (c) cof=0.25. (Left) Color encoded SED_{diff} in the interval [−100%, 100%], and (right) beyond +100%.

remodeling necessarily contain uncertainties and simulations cannot be predictive in a deterministic way. In view of these uncertainties, the generally valid conclusion gains significance for the reliability of implants: the closer the post-operative state comes to the preoperative state in terms of force flow and strain energy distribution, the less are the stimuli to drive remodeling deviating from the pre-THA state. From this bionics perspective the optimal design of an implant is that one which enables force transfer at interfaces and force-transmission through bone that comes closest to the pre-THA state. Then the bone adaptions for a long-term fixation of the implant are minimal. According to this rationale, CO^4 with its force application through the resected surface along with a minor portion of shear force transmission through the stem by friction performs best.

The impact of implant-bone stiffness contrast has been seen as the main reason of stress shielding in the last decades. Consequently, novel materials or structures endowed with a reduced stiffness have been a most active research direction of implant design [4–6]. However, our simulation results indicate that even for a drastic stiffness reduction of the implant material (in the present work to almost 1/20th of the Ti-alloy) stress shielding still persists at some sites. Moreover, for less stiff implant materials additional issues come into play like the choice of the replacement material in view of the required long survival times.

Here, CO^4 turns out to be promising in that stress shielding is almost completely and everywhere avoided, although it is realized by an implant made of a Ti-alloy, such that implant-bone stiffness mismatch persists. The simulation results strongly suggest that stress shielding due to a considerable implant-bone stiffness contrast is only an issue of shear-dominated force transmission. Recall Gefen's precise definition of stress shielding [1] in the introduction, and notice that CO^4 avoids stress shielding by reducing the force interactions between implant and bone to normal forces.

It can be seen as a limitation of our work that only one single data set each of bone structure and for loading was considered, and moreover, that load contributions of muscles and ligaments were neglected though relevant in some aspects of numerical analysis [42]. In this context the question of patient variability arises

[43], and more specifically, whether the close resemblance of post-THA bone loading compared to pre-THA conditions would similarly show up in other cases. Since the newly introduced concept of CO^4 mimics the natural load transfer, the present results shall be transferable, no matter how patient-specific data or loading conditions may differ from the present setting. With the same argument, this transferability shall similarly include different constitutive laws accounting for e.g. anisotropic or inelastic effects.

Several aspects related to CO^4 deserve further analysis, among them the primary and secondary stablility. The porosity and surface roughness of standard implants promotes by friction and by osseointegration the implant's fixation and mechanical locking, which is missing for CO^4. On the other hand, CO^4 strictly blocks implant motion by its collar already right after surgery and maintains the shaft interaction with bone by normal forces. Another important aspect is the impact of variations of implant position on strain and stress distributions [44,45]. Moreover, the bone-prosthesis contact area is worth to be assessed by realistic friction coefficients, at best along with the simulation of the implantation procedure [46].

For the realizability of CO^4 several critical aspects have to be considered. (i) In implantation, additional effort and time have to be invested for consistent geometries of the resection plane adapted to the collar and the hole adapted to the stem, since collar and stem are rigidly connected; here the CO^4 concept exhibits similarities to the thrust-plate endoprosthesis of Huggler & Jacob [9]. In comparison to the standard fixation concept of short stems the additional effort for implant procedure is clearly a drawback of CO^4 in practical application. (ii) For realizing a low-friction regime at the implant-bone interface, a protective thin film of a biocompatible Diamond-Like Carbon (DLC) is favorable and well-established for its excellent bio- and hemocompatibility [47]. Friction coefficients generally in the range of 0.05–0.2 have been reported for DLC [48,49], which are considerably lower than oxidized Ti-alloy surfaces [39]. However, beyond these favorable aspects the relative motion between implant stem and bone in service must prevent the patient from pain. (iii) Another critical requirement for realizing CO^4 is a sufficient quality of cortical bone at the resection plane with respect to stiffness and strength.

5. Conclusion

The salient characteristics of the collar cortex compression concept CO^4 are summarized:

- The CO^4 preserves to an unprecented extent the force flow of pre-surgical bone.
- For its close resemblance to pre-surgical force transmission, bone resorption is not likely to occur for CO^4.
- CO^4 overcomes stress-shielding even for a Ti-based implant, for which the stiffness mismatch to bone persists. The reason is that two crucial conditions are fulfilled by CO^4:
  - activating the resection plane for force transmission by a collar, and
  - avoiding a shear-mediated force transmission at the implant-bone interface by a smooth stem surface for a low friction coefficient.

In conclusion, the present contribution does not wholly question the standard fixation concept of short hip stem implants by shear at the stem site. Reviews indicate for various models competitive survival rates [50], positive results in migration analysis [51], and other promising aspects [52]. Instead, the present analysis has worked out the potential benefits of a collar cortex compression concept CO^4 as a promising alternative load bearing concept for short stem implants. The benefits observed in our simulation analysis but also the critical points and open issues, which we have addressed, can inspire further research in this direction.

Conflict of interest

None.

Funding

None.

Ethical approval

Not required.

Acknowledgements

Assistance of F. Theile in the simulations is acknowledged.

Supplementary material

Supplementary material associated with this article can be found, in the online version, at doi:10.1016/j.medengphy.2018.04.016.

References

[1] Gefen A. Computational simulations of stress shielding and bone resorption around existing and computer-designed orthopaedic screws. Med Biol Eng Comput 2002;40:311–22.
[2] Khanuja HS, Vakil JJ, Goddard MS, Mont MA. Cementless femoral fixation in total hip arthroplasty. J Bone Joint Surg Am 2011;93:500–9.
[3] Falez F, Casella F, Panegrossi G, Favetti F, Barresi C. Perspectives on metaphyseal conservative stems. J Orthop Traumatol 2008;9:49–54.
[4] Huiskes R, Weinans H, Bv R. The relationship between stress shielding and bone resorption arount total hip stems and the effects of flexible materials. Clin Orthop Relat Res 1992;274:124–34.
[5] Kurtz SM, Devine JN. PEEK biomaterials in trauma, orthopedic, and spinal implants. Biomaterials 2007;28:4845–69.
[6] Navarro M, Michiardi A, Castano O, Planell JA. Biomaterials in orthopaedics. J R Soc Interface 2008;5:1137–58.
[7] Gross S, Abel E. A finite element analysis of hollow stemmed hip prostheses as a means of reducing stress shielding of the femur. J Biomech 2001;34:995–1003.
[8] Hazlehurst KB, Wang CJ, Stanford M. A numerical investigation into the influence of the properties of cobalt chrome cellular structures on the load transfer to the the periprosthetic femur following total hip arthroplasty. Med Eng Phys 2014;36:458–66.
[9] Huggler AH, HAC J. The development of the thrust plate prosthesis. In: Morscher EW, editor. Endoprosthetics. Heidelberg: Springer; 1995. p. 248–57.
[10] Taylor WR, H-L P, Clift SE. Bone remodelling of a proximal femur with the thrust plate prosthesis: an *in vitro* case. Comput Methods Biomech Biomed Eng 2004;7:131–7.
[11] Schouten SB, van Winterswijk PJ, Diederix LW, Huij J, Bakx PA. First experiences in 200 thrust plate prosthesis. J Clin Exp Orthop 2016;2:1–6.
[12] Munting E, Verhelpen M. Fixation and effect on bone strain pattern of a stemless hip prosthesis. J Biomech 1995;28:949–61.
[13] Joshi MG, Advani SG, Miller F, Santare MH. Analysis of a femoral hip prosthesis designed to reduce stress shielding. J Biomech 2000;33:1655–62.
[14] University of iowa cerver college of medicine magnetic resonance research facility. The Visible Human Project CT Datasets, https://mri.radiology.uiowa.edu/visible_human_datasets.html, [Accessed 12 October 2016].
[15] U.S. National Library of Medicine (NLM), The Visibile Human Project, https://en.wikipedia.org/wiki/Visible_Human_Project, [Accessed 24 August 2016].
[16] Almeida DF, Ruben RB, Folgado J, Fernandes PR, Audenaert E, Verhegghe B, De Beule M. Fully automatic segmentation of femurs with medullary canal definition in high and in low resolution CT scans. Med Eng Phys 2016;38:1474–80.
[17] Hounsfield GN. Computed medical imaging. J Comput Assist Tomogr 1980;4(5):665–74.
[18] Lutz A, Nackenhorst U. A computational approach on the osseointegration of bone implants based on a bio-active interface theory. Gamm Mitt 2009;2:178–92.
[19] Carter DR, Hayes W. The compressive behavior of bone as a twophase porous structure. J Bone Joint Surg Am 1977;59:954–62.
[20] Morgan EF, Bayraktar HH, Keaveny T. Trabecular bone modulus-density relationship depend on anatomic site. J Biomech 2003;36:897–904.
[21] Austman RL, Milner JS, Holdsworth DW, Dunning CE. The effect of the density–modulus relationship selected to apply material properties in a finite element model of long bone. J Biomech 2008;41:3171–6.

[22] Pegg E. Py_bonemat_abaqus_1.0.3, UK: University of Oxford; 2015. Master's thesis.
[23] Viceconti M, Casali M, Massari B, Cristofolini L, Bassini S, Toni A. The 'standardized femur program' proposal for a reference geometry to be used for the creation of finite element models of the femur. J Biomech 1996;29:1241.
[24] Charité-universitätsmedizin berlin: Orthoload loading of orthopaedic implants. http://www.orthoload.com/database/, [Accessed 27 November 2015].
[25] Damm P, Graichen F, Rohlmann A, Bender A, Bergmann G. Total hip joint prosthesis for in vivo measurement of forces and moments. Med Eng Phys 2010;32:95–100.
[26] Affatato S, Spinelli M, Zavalloni M, Mazzega-Fabbro C, Viceconti M. Tribology and total hip joint replacement: current concepts in mechanical simulation. Med Eng Phys 2008;30:1305–17.
[27] Taylor M, Prendergast PJ. Four decades of finite element analysis of orthopaedic devices: where are we now and what are the opportunities? J Biomech 2015;48:767–78.
[28] Juszczyk MM, Cristofolini L, Viceconti M. The human proximal femur behaves linearly elastic up to failure under physiological loading conditions. J Biomech 2011;44:2259–66.
[29] Grassi L, Väänänen SP, Ristinmaa M, Jurvelin JS, Isaksson H. How accurately can subject-specific finite element models predict strains and strength of human femora? investigation using full-field measurements. J Biomech 2016;49:802–6.
[30] Schileo E, Balistreri L, Grassi L, Cristofolini L, Taddei F. To what extent can linear finite element models of human femora predict failure under stance and fall loading configurations. J Biomech 2014;47:3531–8.
[31] Long M, Rack H. Titanium alloys in total joint replacement – a materials science perspective. Biomaterials 1998;19:1621–39.
[32] Ehrlich PJ, Lanyon L. Mechanical strain and bone cell function: a review. Osteoporos Intl 2002;13:688–700.
[33] Turner CH. Three rules for bone adaptation to mechanical stimuli. Bone 1998;23:399–407.
[34] Kuhl E, Menzel A, Steinmann P. Computational modeling of growth - a critical review, a classification of concepts and two new consistent approaches. Comput Mech 2011;32:71–88.
[35] Ambrosi D, Ateshian GA, Arruda EM, Dumaise J, Goriely A, et al. Perspectives on biological growth and remodeling. J Mech Phys Solids 2011;59:863–83.
[36] Fraldi M, Esposito L, Perrella G, Cutolo A, Cowin S. Topological optimization in hip prosthesis design. Biomech Model Mechanobiol 2010;9:389–402.
[37] Boyle C, Kim IY. Comparison of different hip prosthesis shapes considering micro-level bone remodeling and stress-shielding criteria using three-dimensional design space topology optimization. J Biomech 2011;44:1722–8.
[38] Martin BR, Burr DB, Sharkey NA, Fyhrie DP. Skeletal tissue mechanics. 2nd ed. Heidelberg: Springer; 2015.
[39] Ramos-Saenz CR, Sundaram PA, Diffoot-Carlo N. Tribological properties of ti-based alloys in a simulated bone-implant interface with ringer's solution at fretting contacts. J Mech Behav Biomed Mater 2010;3(8):549–58.
[40] Currey J. Bone strength: what are we trying to measure? Calcif Tissue Int 2001;68:205–10.
[41] T-H C, C-Y L, Cheng C-K. Biomechanical comparison of a new stemless hip prosthesis with different shapes – a finite element analysis. J Med Biol Eng 2009;29:108–13.
[42] Pankaj P. Patient-specific modelling of bone and bone-implant systems: the challenges. Int J Numer Method Biomed Eng 2013;29:233–49.
[43] Taylor M, Bryan R, Galloway F. Accounting for patient variability in finite element analysis of the intact and implanted hip and knee: a review. Int J Numer Method Biomed Eng 2013;29:273–92.
[44] Decking R, Puhl W, Simon U, Claes LE. Changes in strain distribution of loaded proximal femora caused by different types of cementless femoral stems. Clin Biomech 2006;21:495–501.
[45] Zanetti EM, Audenino AL. Differential thermography for experimental, full-field stress analysis of hip arthroplasty. J Mech Med Biol 2010;10(3):515–29.
[46] Zanetti EM, Bignardi C. Mock-up in hip arthroplasty pre-operative planning. Acta Bioeng Biomech 2013;15(3):123–8.
[47] Robertson J. Diamond-like amorphous carbon. Mater Sci Eng R 2002;37:129–281.
[48] Grill A. Tribology of diamondlike carbon and related materials: an updated review. Surf Coat Tech 1997;507–13:94–5.
[49] Erdemir A, Donnet C. Tribology of diamond, diamond-like carbon, and related films. In: Bhushan B, editor. Handbook of Modern Tribology, Vol. 2. Materials Coatings, Boca Raton. Florida: CRC Press; 2001.
[50] van Oldenrijk J, Molleman J, Klaver M, Poolman RW, Haverkamp D. Revision rate after short-stem total hip arthroplasty. Acta Orthop 2014;85:250–8.
[51] Schmidutz F, Graf T, Mazoochian F, Fottner A, Bauer-Melnyk A, Jansson V. Migration analysis of a metaphyseal anchored short-stem hip prosthesis. Acta Orthop 2012;83:360–5.
[52] Floerkemeier T, Tscheuschner N, Calliess T, Ezechieli M, Floerkemeier S, Budde S. Cementless short stem hip arthroplasty METHA as an encouraging option in adults with osteonecrosis of the femoral head. Arch Orthop Trauma Surg 2012;132:1125–31.